

Fluidic Control of a Turret Wake: Aerodynamic and Aero-Optical Effects

Bojan Vukasinovic* and Ari Glezer*

Georgia Institute of Technology, Atlanta, Georgia 30332-0405

Stanislav Gordeyev† and Eric Jumper‡

University of Notre Dame, Notre Dame, Indiana 46556

and

Valdis Kibens‡

The Boeing Company, Saint Louis, Missouri 63166

DOI: 10.2514/1.J050085

Effects of direct small-scale actuation on aerodynamic and aero-optical characteristics of flow over a hemisphere-on-cylinder turret model ($D = 0.61$ m) with a round 0.254-m-diam conformal optical aperture are investigated at $M = 0.3$ and $Re_D = 4.46 \cdot 10^6$ (with additional measurements at $M = 0.4$ and 0.5). Flow control is effected by arrays of piezoelectrically driven synthetic jet modules. The cumulative effect of the actuation is manifested by a concomitant delay of flow separation and active, dissipative suppression of turbulent motion downstream of separation. Effects of actuation on aero-optical distortions are assessed from the flow dynamics, using surface oil visualization, static pressure distributions, and hot-film measurements within the separated flow domain. In addition, the suppression of optical distortion across the separated flow is measured directly using a Malley probe over a range of elevation angles. These measurements show that for a fixed actuation level, the active suppression level of spectral components of the optical distortion is about 30% within a resolved frequency band $0.5 < f < 25$ kHz at $M = 0.3$.

Nomenclature

Ap	= aperture size
A_j	= exit area of the actuator orifice
A_o	= frontal turret area
C_p	= pressure coefficient
C_μ	= jet momentum coefficient
D	= turret diameter
f_d	= actuation frequency
I	= far-field intensity
I_0	= diffraction-limited intensity
k	= turbulent kinetic energy
M	= Mach number
OPD	= optical path difference
OPD _{rms}	= root-mean-square of optical path difference
R	= turret radius
Re_D	= Reynolds number
St_D	= Strouhal number
U_0	= freestream velocity
U_j	= average jet velocity
\bar{W}_{rms}	= wave-front mean-removed spatial root-mean-square
H	= height of turret base
β	= azimuthal angle of pressure ports
γ	= elevation angle of optical aperture
γ_s	= flow separation angle
δ	= incoming boundary-layer thickness
λ	= wavelength
ρ	= local air density

ρ_∞	= freestream air density
ρ_{SL}	= sea-level air density (1.225 kg/m ³)
θ	= shear-layer characteristic scale

I. Introduction

TURRETS provide convenient housing for pointing and tracking laser beams from airborne platforms. However, a turret creates a separated turbulent region in the flow, which, even at relatively low subsonic speeds, starts to distort an otherwise planar emerging laser beam (e.g., [1–3]). This, in turn, leads to the laser beam's unsteady defocusing and jitter at the target [4]. Control of flow over a bluff-body turret that houses a laser-based optical system must satisfy more demanding requirements in comparison to separation control over external aerodynamic surfaces. Whereas the effectiveness of the flow control method on aerodynamic surfaces can be evaluated in terms of its effect on the time-averaged aerodynamic forces and moments, the metric becomes much more stringent when the intent of flow control is to enhance transmission of optical wave fronts through regions of separated turbulent flow. When an optical wave front passes through a variable index-of-refraction turbulent flow near an aerodynamic surface (boundary layers, separated shear layers and wakes), its wave front becomes distorted or aberated and these distortions are referred to as sources of *aero-optical problems* [4]. These wave-front distortions combined with optical aberrations caused by the wave-front propagation through the atmosphere, referred to as sources of *atmospheric propagation problems* [5], ultimately degrade the light intensity from the otherwise diffraction-limited intensity at the destination. These aberrations have high spatial and temporal bandwidths that are well outside the current capabilities of traditional adaptive-optic methods [6]. Separated shear layers are particularly destructive because of the presence of coherent vortical structures that induce strong pressure and density gradients [7]. Left untreated, these shear-layer-related optical aberrations can limit an airborne transmitting system solely to a forward-looking quadrant. To extend viewing angles to at least a portion of an aft-looking quadrant, one can extend the region of the attached flow by delaying the separation of the shear layer and/or disrupting formation of the large-scale shear layer vortices. The intent of the work presented in this paper is to evaluate the effectiveness of a strategy for achieving significant

Presented as Papers 2009-0816 and 2009-0817 at the 47th AIAA Aerospace Sciences Meeting and Exhibit, Orlando, FL, 5–8 January 2009; received 23 July 2009; revision received 10 February 2010; accepted for publication 10 April 2010. Copyright © 2010 by B. Vukasinovic, A. Glezer, S. Gordeyev, E. Jumper, and V. Kibens. Published by the American Institute of Aeronautics and Astronautics, Inc., with permission. All rights reserved. Copies of this paper may be made for personal or internal use, on condition that the copier pay the \$10.00 per-copy fee to the Copyright Clearance Center, Inc., 222 Rosewood Drive, Danvers, MA 01923; include the code 0001-1452/10 and \$10.00 in correspondence with the CCC.

*Woodruff School of Mechanical Engineering.

†Department of Aerospace and Mechanical Engineering.

‡Mail Code S306-430, P.O. Box 516.

improvement in light transmission efficiency by minimizing laser wave-front degradation through active flow control attenuation of the unsteady aerodynamic environment, which, if left untreated, leads to serious degradation of the optical environment in uncontrolled flow.

Traditional active methods for controlling separation over lifting surfaces and bluff bodies make use of unstable frequency. Introducing perturbation signals at the nominal (dimensionless) frequency $St = O[1]$ upstream of the region of separation results in enhanced entrainment and a Coanda-like deflection of the flow toward the adjacent aerodynamic surface. However, the deflected flow can separate again depending on the modified streamwise pressure gradients along the surface. Resulting in considerable changes in global aerodynamic forces, this method can degrade an optical signal that is transmitted through the affected region perhaps even beyond the levels observed in the absence of control. A body of work studying the control of separation by the application of actuation at frequencies that are at least an order of magnitude higher than the unstable frequency of the shear layer suggests that high-frequency actuation makes it possible to achieve attached flows in which large coherent vertical motions that are associated with low-frequency actuation are largely suppressed (e.g., [8,9]).

Some previous work on separated flows over a three-dimensional bluff-body configuration has been directly motivated by the aero-optical problems involving an aircraft turret. Such a configuration has typically consisted of a cylindrical base having a hemispherical cap with a flat or a conformal aperture. The resulting flowfield is fairly complex as shown by de Jonckheere et al. [10]. It has been shown [2,3,11] that the main cause of aero-optical distortions for moderate back-looking angles is the shear-layer architecture that forms shortly after the flow separates from the hemispherical portion of the turret. Investigations of flow control on these configurations included the effect of suction on the wake structure [12] and the addition of aft-mounted fairings and splitter plates [13]. The former showed significant alteration of the wake structure even at low levels of suction, whereas the latter presented reduction of the baseline drag up to 55% by using a large fairing. The separated flow behind the turret with a flat aperture and the effects of passive control on the optical aberrations were characterized by Gordeyev et al. [14] and Cress et al. [11], and the aerodynamical and aero-optical characterization of the baseline flowfield over a conformal-aperture turret configuration was investigated by Gordeyev et al. [3]. There have been few investigations of generic surface-mounted hemispheres at high Reynolds numbers. In a numerical investigation of winds over hemispherical domes, Manhart [15] found that a Kármán-like vortex train is shed from the hemisphere. In these flows, however, the thickness of the upstream boundary layer is comparable to the hemisphere radius, unlike the flow over an aircraft turret for which the oncoming boundary-layer thickness is much smaller than the turret radius. Another limiting case, when the cylindrical base is much higher than the hemisphere radius was investigated by Leder et al. [16] ($H = 3R$). They characterized the wake behind such a high-aspect-ratio turret and showed that it is dominated by vortices shed off the cylindrical support. The effectiveness of direct, high-frequency control ($St_D > 10$) of the separated flow over a hemispherical turret on a flat plate with a thin upstream boundary layer was demonstrated by Vukasinovic et al. [17] at $Re_D = 4 \cdot 7 \cdot 10^5$. These authors showed that the presence of flow control can substantially reduce the extent of the recirculating domain downstream of the hemisphere with significant reduction in turbulent kinetic energy. Vukasinovic et al. [18] simultaneously measured the aerodynamic and aero-optical environments within the separated flow off a hemispherical turret at freestream Mach numbers up to $M = 0.64$. They reported significant suppression of turbulent fluctuations and reduction in optical distortions up to $M = 0.45$ by the active flow control method where reduction in optical distortions at $M = 0.4$ was reported up to 45%. Recently, Wozidlo et al. [19] reported separation delay and turbulence intensity reduction within the wake of a hemispherical shell by means of base suction and upstream passive vortex generators at $Re_D \leq 3 \times 10^5$. Vukasinovic and Glezer [20] demonstrated the effectiveness of fluidic, direct high-frequency control in turbulence suppression behind a bluff-body

turret at $Re_D = 8 \times 10^5$. Morgan and Visbal [21] presented numerical simulation of the separation delay over a turret at $M = 0.4$ and $Re_D = 2.4 \times 10^6$, and concluded that either localized or distributed suction resulted in significant separation delay and suppression of large-scale structures in the wake. Besides the studies of active flow control over a conformal turret aperture, recent studies explored synthetic jet effectiveness in the flow control over a flat turret aperture [22–24]. They reported reduction in the flow unsteadiness in a case of the open-loop control [22], and further improvement in the control effect in the closed-loop control based on feedback from the surface-distributed dynamic pressure sensors [23,24].

The present paper reports effects of direct small-scale excitation on aerodynamic and aero-optical characteristics within the near wake of a hemisphere-on-cylinder turret model. Pretest high-fidelity baseline flow simulations at The Boeing Company (not shown) indicated that the oncoming boundary-layer thickness on the support surface was about one-twelfth of the turret radius, which is similar to the ratio for the airborne turret. Actuation using arrays of synthetic jet actuators placed upstream of the turret aperture results in concomitant delay of flow separation and active, dissipative suppression of turbulent motions within the separated shear layer. The effects of actuation are investigated over a range of optical aperture elevation angles and are characterized using surface pressure measurements and hot-film anemometry within the separated flow. In addition, direct measurements of aero-optical distortions are assessed using Malley probe measurements. While the primary objective of the current work is to estimate the effectiveness of active flow control for suppression of optical aberrations at $M = 0.3$, its control effectiveness was also assessed at $M = 0.4$ and 0.5 . The experimental setup and procedures are described in Sec. II. The characterization of the base flow is described in Sec. III, and Sec. IV presents the results of controlled flow, and finally, the conclusions are presented in Sec. V.

II. Experimental Setup and Diagnostics Procedures

All experiments were conducted at the Subsonic Aerodynamic Research Laboratory (SARL) facility at the Wright-Patterson Air Force Base. The SARL facility has an open-loop wind tunnel with a

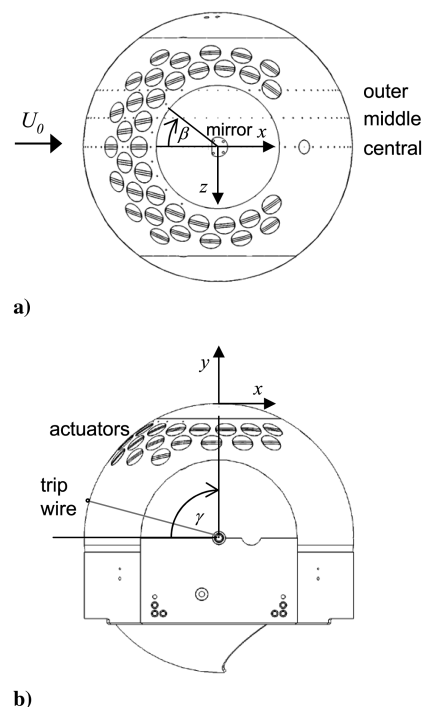


Fig. 1 Views of a) top and b) side of the 0.61-m-diam turret model having a 0.254 m instrumented spherical cap in place of an optical aperture.

2.1 × 3 m octagonal test section that is 4.6 m long. Mach number can be varied between 0.2 and 0.5. The test section was designed for maximal optical access, having 28 windows built into the test-section walls; they comprise 56% of the test-section surface area. The tunnel has a 14 × 15.2 m inlet, giving a 35:1 contraction ratio. Honeycomb and screens are installed in the inlet before the contraction for turbulence intensity management.

The turret model is shown in Figure 1. It measures 0.61 m in diameter, and is equipped with a 0.254-m-diam spherical aperture insert that models a conformal optical aperture. This area is unavailable for the flow control hardware. The tunnel blockage imposed by the turret was 4.2%. While the cylindrical turret base ($H/R = 0.625$) remains stationary, the spherical portion of the turret can be rotated about the z axis for about 53° , thus allowing variation in the aperture's elevation angle γ (defined as the angular position of the aperture's centerline, relative to the freestream). The spherical portion of the turret is instrumented with static pressure ports that are distributed along central, middle (20° off centerline), and the outer (40° off centerline) planes (Fig. 1), which include 39, 44, and 39 ports, respectively. In addition to these main pressure ports, nine static pressure ports also are distributed just upstream from the optical aperture, so that the middle port is in the central plane, and four pressure ports are distributed over each half of the aperture, having azimuthal angles $\beta = 12.5, 25.6, 39.7, \text{ and } 57.7^\circ$. These additional nine ports are used to assess the flow symmetry and spanwise (z direction) effects of the actuation. All static pressure measurements were done by a dedicated PSI Netscanner system, and the averaged pressure profiles were based on 320 individual data sets, such that uncertainty of the average is estimated to be less than 1%.

A total of 36 individually addressable actuators are distributed in three rows around the aperture circumference, such that the first row (closest to the aperture) consists of 15, the second of 14, and the third of 7 actuators (Fig. 1). Each actuator module has a high-aspect-ratio rectangular jet orifice (measuring 38.1×0.5 mm) integrated into a 48-mm-diam cylindrical body that can be rotated about its own axis to allow different orientations of the jet orifice relative to the freestream, thus enabling predominantly streamwise or spanwise

vorticity generation upon jet activation. Previous studies suggested possible advantages of the manipulation of spanwise vorticity concentrations in incompressible flows [20] and of streamwise vorticity in compressible flows [18]. In the preliminary stages of the present investigation several combinations of orifice orientations were tested (i.e., aligned with the freestream, approximately with the local flow, and normal to the freestream); based on these tests it was decided to arrange orifices approximately aligned with the freestream. Since the actuators move with the spherical part of the turret and the optical aperture, their position relative to the point of separation changes and therefore different actuator arrays can be activated depending on the aperture position. In the present experiments, the actuation frequency was kept at $f_d = 1600$ Hz, and the actuation strength was varied over a range of $3 \times 10^{-6} < C_\mu < 1.5 \times 10^{-5}$ per single active actuator, as the jet momentum coefficient is defined as $C_\mu = \rho_j U_j^2 A_j / (\rho_0 U_0^2 A_o)$, where A_j is the total jet orifice area, A_o is frontal projection of the turret, and U_j is the average jet velocity during the expulsion part of the cycle. Based on laboratory experiments, it is known that operational cavity temperature of the present actuator is higher than that of the surrounding air (by less than 20°C). As the actual jet temperature could not be measured in the tunnel tests, an approximation $\rho_j \approx \rho_0$ is used in calculation of C_μ , which thereby overstates C_μ by several percent. Hence, this approximation can be seen as setting the upper limit on C_μ . Control effectiveness was assessed using both the full 36 actuator configuration (maximum $C_\mu = 5.6 \times 10^{-4}$) and the center 24 actuators (maximum $C_\mu = 3.7 \times 10^{-4}$). The former is labeled as case 1 and the latter is case 2 in the remainder of the paper.

Spectral characterization of the baseline (nonactuated) and actuated flows were accomplished using single-sensor hot-film anemometry. For that purpose, four hot-film probes were mounted on retractable holders and stowed in tunnel surface wall depressions when not in use. During the measurements, only one probe at a time was elevated from the surface and positioned at the measurement location, where the cross-stream measurement locations were selected so that the local shear layer thickness was traversed. The sensor streamwise positions are $x/R = 0.5$ (HW1), 1 (HW2), 1.5 (HW3), and 2 (HW4), where the streamwise distance x is measured from the hemisphere center (Fig. 1). All measurement locations are shown in Fig. 2, where the cross-stream measurement locations were selected to be within the local shear layer width. Each set of measurements consisted of 80 individual time traces that resulted in 1.8 Hz resolution in the frequency domain. During data postprocessing, only velocity fluctuations were extracted from the measured time traces, which were then processed by spectral analysis. Uncertainty in the resulting averaged spectra is estimated to be 5%.

The turret position in the tunnel was driven by the aero-optical measurements at far looking-back angles and a need to emulate supporting surface at the turret base. Hence, it was mounted on the tunnel sidewall upstream from the test-section center, as can be seen in Fig. 3b. To check the impact of the turret position on its aerodynamic performance, high-fidelity numerical simulations were done at Boeing (not published) that compared the baseline flow over

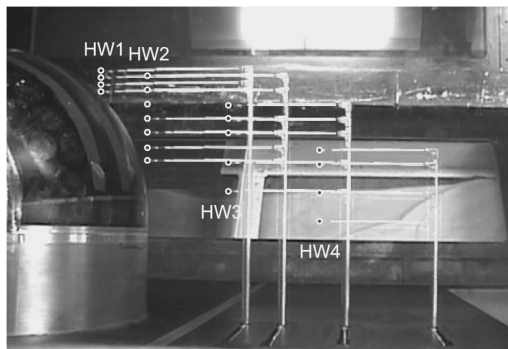


Fig. 2 Overlapped measurement positions of four hot-film sensors downstream from the turret.

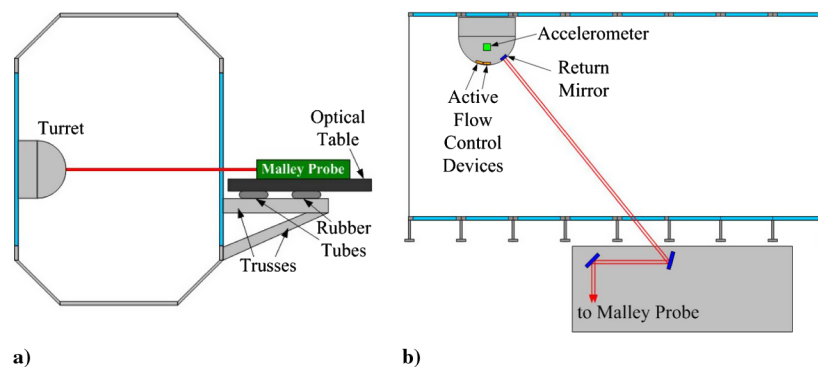


Fig. 3 Optical table arrangement: a) side and b) top views.

the turret in this test position to the same turret in the free outer flow (only with the support surface present). Only minor differences in the major flow characteristics were found (locations of the separation and reattachment lines) and recirculating bubble cores differed by single percentages.

To minimize tunnel-induced mechanical vibrations and relative motion between the turret and the optical bench, inflatable donut shaped isolators were placed between the optical table and trusses holding the optical bench, as shown in Fig. 3a, and they were shown to be effective in significantly reducing the bench's vibrational motion. The turret did not have a vibration-isolation system, as the level of mechanical vibration of the turret was measured using the accelerometer and found to be less than the residual vibrations of the optical bench. The combined vibration-related jitter from the optical table and the turret was removed from the data in the postprocessing analysis as described later.

Optical measurements were performed at the turret center plane (i.e., zenith plane) at four aperture elevation angles $\gamma = 129, 137, 143,$ and 148° using the Malley probe (MP). The Malley probe is described in detail by Gordeyev et al. [2]; it uses two parallel small-aperture laser beams to measure one-dimensional slices of optical wave fronts in the streamwise direction. Regular Plexiglas windows in the tunnel walls ordinarily would be unacceptable for making optical measurements; however, the Malley probe was able to make optical measurements through these windows because they did not impose significant optical distortions on the small 1-mm-diam Malley-probe beams. A round 25.4-mm-diam return mirror was mounted flush on the cap center and two Malley probe He-Ne laser beams were transmitted into the test section using a series of steering mirrors. After reflecting off the surface-embedded return mirror, the beams were reflected back to the optical bench along the same optical path, as shown schematically in Fig. 3b. This approach in conducting the Malley probe measurements allows the laser beams to go along the same flow twice, doubling the signal-to-noise ratio and significantly simplifying the optical setup. The Malley-probe laser beams were separated by approximately 7 mm in the streamwise direction. Optical aberrations at selected elevation angles were measured by recording high-bandwidth time-resolved deflection angles (jitter) of the laser beams using position sensing devices. The sampling frequency used was 50 kHz, and sampling times of 20 s were made for each measurement case.

The Malley probe data were processed as follows:

- 1) Measure streamwise deflection jitter angles $\theta_1(t)$ and $\theta_2(t)$.
- 2) Compute a cross-correlation function $S(f)$, $S(f) = \langle \hat{\theta}_1^*(f) \hat{\theta}_2(f) \rangle$, where square brackets denote ensemble averaging and asterisk denotes complex conjugate.
- 3) Calculate convective speed, U_c , by calculating the time delay between the two jitter signals using the spectral method described by Gordeyev et al. [2].
- 4) Compute jitter power spectra $P_\theta(f) = \langle |\hat{\theta}(f)|^2 \rangle$ for each jitter signal.

5) Remove vibration contamination by analyzing the jitter-angle spectra $P_\theta(f)$ and the phase of the cross-correlation function, $\text{Arg}[S(f)]$, and applying a high-pass filter $F(f)$, as described in Appendix A.

6) Calculate a time-varying 1-D wave-front slice, $\text{OPD}(t)$, assuming the frozen-flow hypothesis:

$$\text{OPD}(t) = -U_c \int \theta_1(t) dt$$

7) Apply an aperture, A_p , to $\text{OPD}(t)$ results, remove instantaneous tilt components from each apertured slice and calculate the residual OPD_{rms} average over all ensembles for a given aperture. A_p was chosen to be 1/3 of the hemisphere diameter, $A_p = 0.2$ m.

An alternative way to compute OPD_{rms} directly from the deflection-angle spectrum is presented in Appendix A.

III. Baseline Flow

Earlier investigations (e.g., [3,10,18]) have demonstrated that the topology of the baseline turret flow is rather complex and Mach- and Reynolds-number-dependent. To avoid changes in separation location and dynamics that are associated with the flow transition, the hemisphere's boundary layer in the present experiments was tripped using a 0.2-mm-diam wire that was attached to the surface with a 0.1 mm tape along meridional plane at a 15° elevation relative to the center (symmetry) plane of the hemisphere (Fig. 1). The trip wire was used to maintain exactly the same baseline flow separation regardless of the turret elevation angle, as slight, but consistent, shift in the separation position was measured without the tripping source. Such a change in separation position can be attributed to even the minute steps at the surface interfaces, as the rest of the hemisphere surface was remarkably smooth. The trip wire did not move with the turret rotation, i.e., it was repositioned at each turret elevation angle change.

The tripped baseline flows are first characterized using measurements of static pressure distributions in the central, middle and outer planes shown in Fig. 1. The pressure profiles in these three planes are shown in Fig. 4 for aperture elevation angles $\gamma = 129^\circ, 137, 143,$ and 148° , and $M = 0.3, 0.4,$ and 0.5 . These pressure profiles suggest that, for a given Mach number, the separation points in each of the three measurement planes nearly coincide at the planes' own reference angles, indicating that the flow separates first over the outer edges of the optical aperture and remains attached farthest in the central plane. This observation is in accord with previous data reported for the flow over a hemispherical turret [18]. The present measurements also suggest that the separation angle in all planes shifts slightly upstream with increasing M , such that the flow separates just upstream from 120° in the central plane at $M = 0.3$, and at $M = 0.5$, the separation point is at about $\gamma_s = 115^\circ$ (see inset in Fig. 4a). Perhaps the most interesting view of the baseline flow

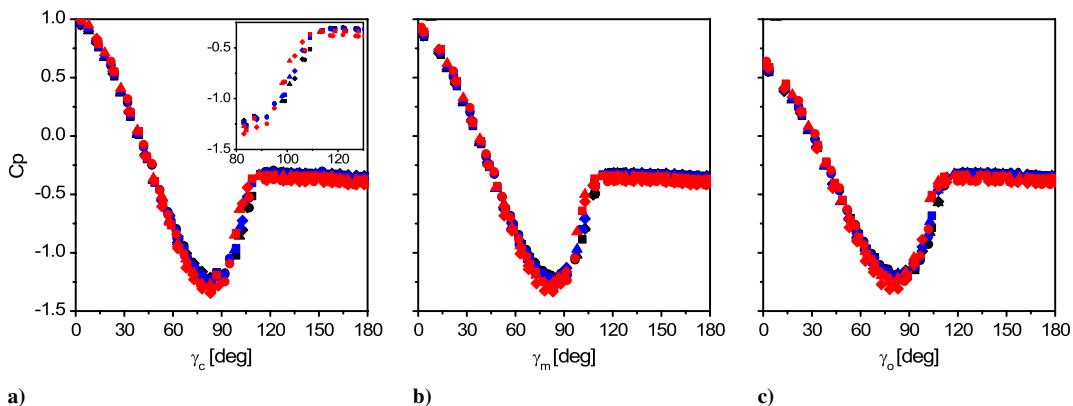


Fig. 4 Overlapped static pressure measurements at aperture elevation angles $\gamma = 129$ (square), 137 (circle), 143 (triangle), and 148° (diamond), and baseline flows at $M = 0.3, 0.4,$ and 0.5 in the a) central, b) middle, and c) outer planes.

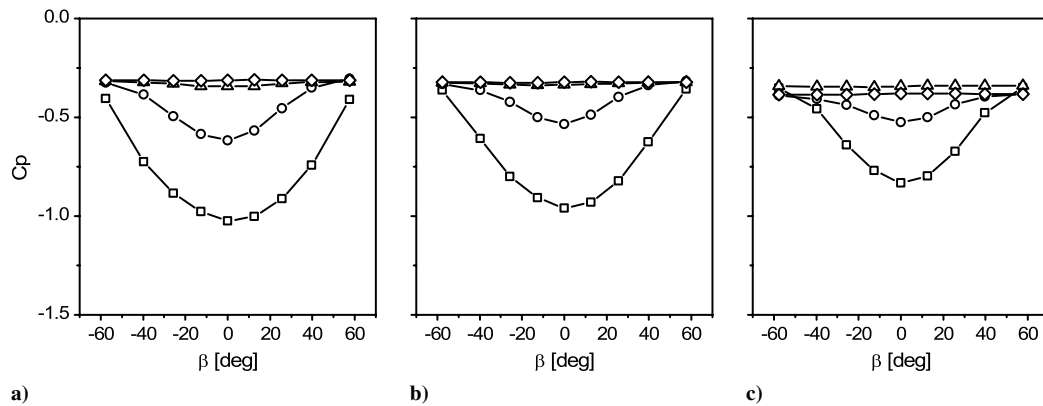


Fig. 5 Pressure distributions about the optical aperture center ($\beta = 0^\circ$) at elevation angles $\gamma = 129$ (square), 137 (circle), 143 (triangle), and 148° (diamond), for the baseline flows at a) $M = 0.3$, b) 0.4 , and c) 0.5 .

over the optical aperture is shown in Fig. 5 that includes pressure distributions along the upstream edge of the aperture (cf., Fig. 1) for $\gamma = 129, 137, 143$, and 148° , and $M = 0.3, 0.4$, and 0.5 . These data show that in all of the cases the flow remains remarkably symmetric about the streamwise centerline of the aperture ($\beta = 0^\circ$). When the flow is not separated at the upstream edge of the aperture ($\gamma = 129$ and 137°), the pressure has a minimum at the aperture center, and increases toward the spanwise edges of the turret. The pressure profiles at $\gamma = 137^\circ$ indicate presence of a separated flow at the outer upstream edges of the optical aperture, and at $\gamma = 143$ and 148° , regardless of M , the flow approaching the optical aperture is already separated over the measurement domain. The upstream shift in the separation line with increasing M is also apparent in the pressure distributions at the lowest elevation angle, where the approaching flow is attached at $M = 0.3$ and separated at $M = 0.5$.

A global topology of the baseline flow at $M = 0.3$ was investigated using surface oil-flow visualization. The main footprint of the flow was visualized over the flat surface of the supporting turret wall, and additional visualization was performed along the cylindrical turret base. The recorded images of the surface oil visualization showed that the baseline flow over the turret is quite symmetric. Some features of the flow that were deduced from the series of partial snapshots and direct measurements off the surfaces are shown schematically in Figs. 6a (the turret support plane) and 6b (the cylindrical surface). As the oncoming boundary layer approaches the adverse pressure gradient induced by the presence of the cylinder base, a spanwise (necklace) vortex is formed that becomes strained and deformed under the modified pressure field, giving a rise to the streamwise vortex branches along each spanwise edge of the cylinder. A stagnation point is formed at $0.5R$ upstream from the turret, the outer flow is displaced by the bluff body, accelerates over the hemisphere surface and around the cylindrical surface until the adverse pressure gradients on the aft sides induce separation. The flow footprints shown schematically in Fig. 6a indicate that the flow separates off the cylinder base near its apex and spreads azimuthally

by approximately 120° . The visualization on the surface of the cylinder in Fig. 6b indicates the 3-D nature of the separating flow near the cylinder's base, as well as its localized, near-wall effect. Further away from the support wall, the flow trajectories over the cylinder become displaced toward the hemispherical part of the turret, and merge into a separation line. This visualization supports the assessment, based on the static pressure measurements (Figs. 4 and 5), that the flow separates first at the spanwise edges of the turret and remains attached farthest in the (center) plane of symmetry. The ensuing separated flow off the turret surface has a main central wake that reattaches to the support wall at approximately $1.3R$ downstream from the turret back edge, and two additional near-wall wake segments that appear to be associated with the vortices that are shed off each side of the cylindrical support. After initial narrowing, the main wake begins to spread as shown in Fig. 6a. It appears that the overall wake dynamics is dominated by the flow separation off the hemispherical part of the turret, whereas the separation off the relatively short cylinder base has a limited effect on the wake. In contrast to this observation, measurements in a high-aspect-ratio turret [16] where cylindrical base is much taller than its radius, the near wake is dominated by the dynamics of the vortices shed off the cylinder.

Baseline (i.e., turret with no active flow control) Malley probe jitter/beam-deflection-angle spectra for different elevation angles as a function of the incoming Mach number are presented in Fig. 7. The analysis of the phase of the cross-correlation function, $\text{Arg}[S(f)]$, (not shown) revealed that the series of peaks at low frequencies, below 500 Hz, is the result of mechanical vibrations of the tunnel, the turret, and to a lesser degree the optical bench. For a fixed Mach number, spectra are approximately the same at a range of low frequencies between 80 and 300 Hz, indicating strong tunnel-related mechanical vibrations, which should be independent of the elevation angle. The main vibrational peak is related to the tunnel blade passage speed that was approximately 155 Hz for $M = 0.3$, 200 Hz for $M = 0.4$, and 250 Hz for $M = 0.5$. Harmonics of the main

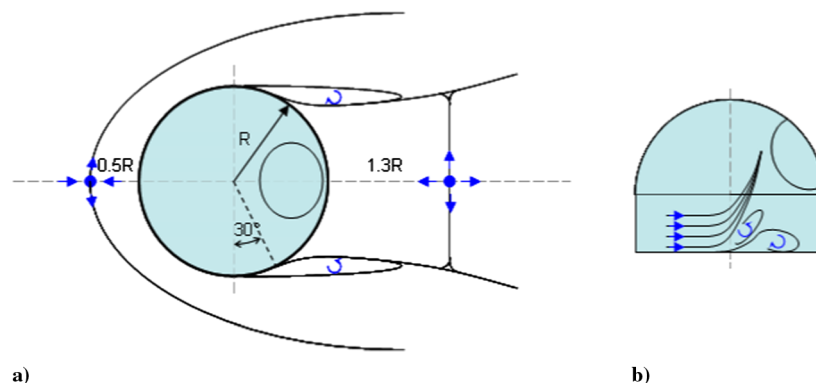


Fig. 6 Schematics of the surface oil-flow visualization of the baseline flow at $M = 0.3$ at the a) support wall and b) cylindrical surface of the turret.

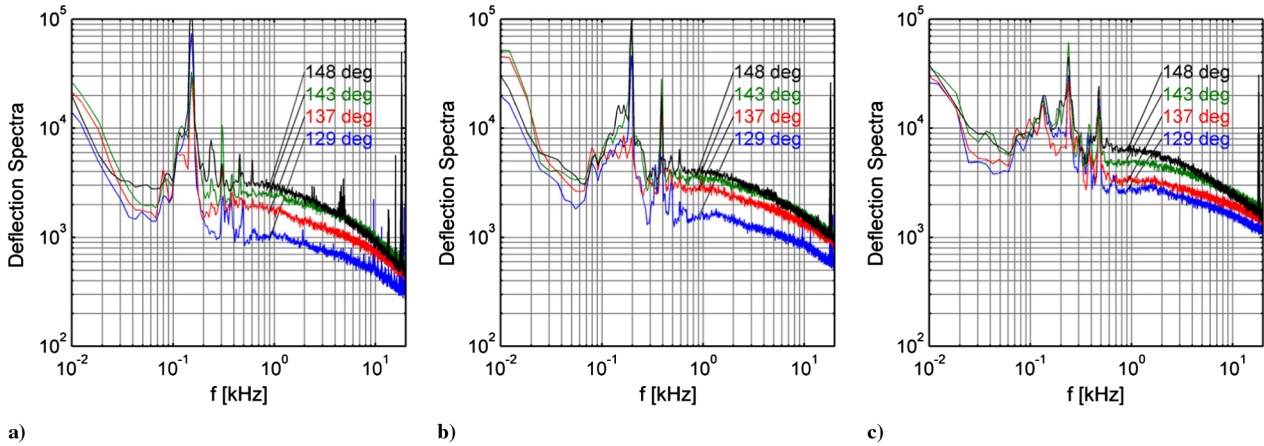


Fig. 7 Optical deflection/jitter-angle spectra as a function of the elevation angle for a) $M = 0.3$, b) 0.4 , and c) 0.5 .

vibrational peak can also be observed in jitter spectra. These vibrations overwhelm the optical signal at these frequencies, especially around the main vibrational peak, and make the data corrupted and therefore mostly unusable over these ranges of frequencies. Above 500 Hz the optical signal shows a broad hump that indicates the presence of the shear layer behind the turret. For the elevation angle of $\gamma = 129^\circ$, the frequency location of this hump increases from approximately 1 to 2 kHz, increasing with Mach number. This characteristic is expected for the shear layer, since the most unstable shear-layer frequency is proportional to the freestream speed. The corresponding Strouhal number was found to be approximately constant, $St = f_{peak} D / U_0 = 4.5$. It confirms the fluid mechanic conclusion that, in the absence of flow control, the Malley-probe beams encounter separated flow at the smallest of the four elevation angles. The location of the shear-layer-related peak moves toward lower frequencies with increasing the elevation angle, from 1 to 0.5 kHz for $M = 0.3$, from 1.3 to 0.8 for $M = 0.4$, and from 1.8 to 0.9 kHz for $M = 0.5$. This observation indicates that the shear layer grows downstream from the separation location, which is consistent with the flow mechanics of the spatially-evolving shear layer. Intensities of the spectra increase with the Mach number, as the jitter/deflection-angle spectra for a shear layer separated off a turret have been previously shown to follow a ρM^2 law [2,3,18]. The present spectra further validate this scaling law. Finally, the spectra monotonically increase with increasing the elevation angle, indicating that the optical aberrations caused by the shear layer become stronger with increasing looking-back angle, which is consistent with the expected optical character of the shear layer.

All the observed trends in the jitter spectra are quite similar to results for optical jitter/deflection-angle spectra around hemispheres [18]. The increasing optical signal with the elevation angle going up is not only due to the shear layer structures growing downstream (i.e., for a greater looking-back angle) but also because of the fact that the laser beam is traversing the shear layer at ever-higher oblique angles, increasing its optical propagation path length due to oblique propagation.

The OPD_{rms} results, computed as described in the end of Sec. II for the baseline flows are plotted in Fig. 8a versus $\rho / \rho_{SL} M^2$ (ρ_{SL} is sea-level density) for different elevation angles. As can be seen in Fig. 8a for all elevation angles OPD_{rms} approximately follows the ρM^2 dependence.

In general, optical aberrations around turrets depend on an incoming boundary layer δ , a typical vortical structure size/scale θ , a turret diameter D , a beam aperture A_p , a freestream density ρ_∞ , and a freestream Mach number M :

$$OPD_{rms} = f(\delta, \theta, D, A_p, \rho_\infty, M)$$

Applying dimensional analysis and recognizing that $OPD_{rms} \sim \rho M^2$, we obtain the following relationship for the OPD_{rms} :

$$\frac{OPD_{rms}}{D} = \frac{\theta \rho_\infty}{D \rho_{SL}} M^2 g\left(\frac{A_p}{D}, \frac{\delta}{D}\right)$$

The shear layer structure size is proportional to the boundary-layer thickness on top of the turret before the separation off the turret. It is reasonable to assume that the most of the incoming boundary layer is wrapped up into the necklace vortex and the boundary layer starts to regrow from the stagnation point in the front of the turret. Therefore, the boundary-layer thickness *on the top of the turret* is proportional to

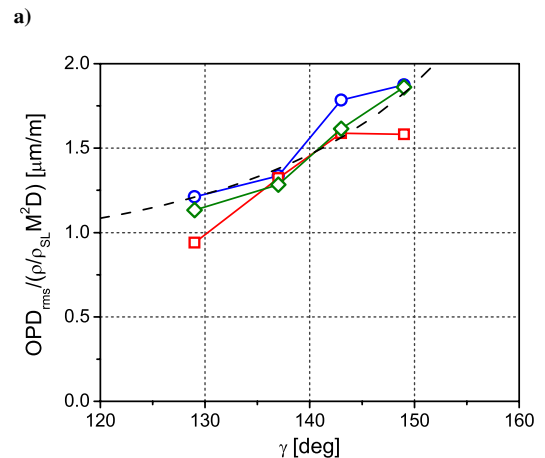
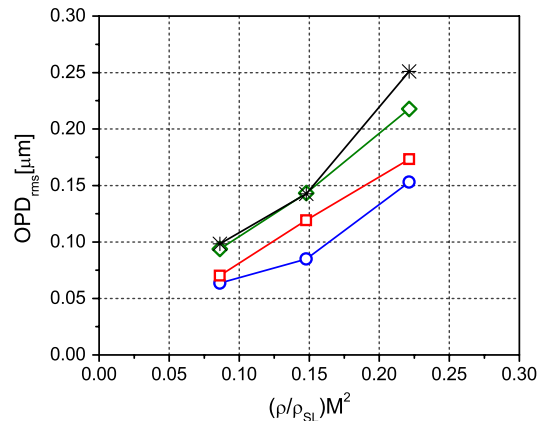


Fig. 8 Plots of a) baseline OPD_{rms} as a function of $\rho / \rho_{SL} M^2$ for different elevation angles $\gamma = 129$ (circle), 137 (square), 143 (diamond), and 149° (*), and b) baseline optical data replotted in a self-similar form, $OPD_{rms} / (\rho M^2 D)$ as a function of elevation angles for all Mach numbers $M = 0.3$ (circle), 0.4 (square), and 0.5 (diamond). $1 / \sin(\gamma)$ is plotted as a reference (dashed line).

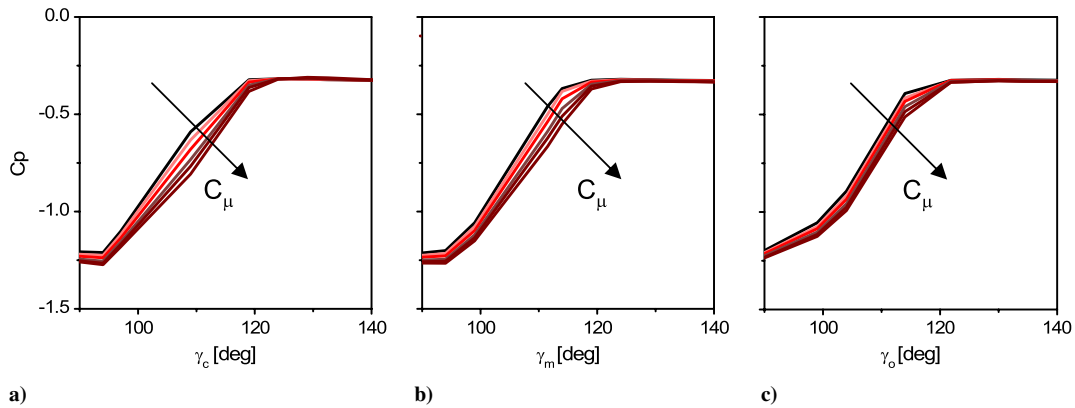


Fig. 9 Static pressure profiles for the baseline flow (black) at $M = 0.3$ and $\gamma = 139^\circ$ and controlled flows in the a) central, b) middle, and c) outer planes. Controlled pressure profiles shift to the right, directly proportional to the jet momentum coefficient.

the turret diameter, and $\theta/D = \text{const}$. Also, for sufficiently small incoming boundary layer, the separated flow behind the turret exhibits the *global* self-similar evolution and thus is insensitive to the *local* value of δ , assuming the incoming boundary does not affect the typical flow structure size sufficiently downstream from the separation point. Numerical simulations done at Boeing (not shown) of the present baseline flow indicated that the boundary-layer thickness at the turret apex is about 3 mm at $M = 0.3$, which supports the assumption that $\delta \ll D$. If the relative aperture A_p/D is kept the same, than the above equation shows that $\text{OPD}_{\text{rms}} \sim \rho M^2 D$.

To check this self-similarity, the optical results are replotted in Fig. 8b in a self-similar form, $\text{OPD}_{\text{rms}}/((\rho/\rho_{\text{SL}})M^2D)$, versus the elevation angle, γ , for all Mach numbers. Also, the oblique angle effect [18], $\text{OPD}_{\text{rms}} \sim 1/\sin(\gamma)$ is shown in Fig. 8b as a dashed line. For all Mach numbers and elevation angles the data approximately collapse about $1/\sin(\gamma)$ curve, giving additional validity to the comment made earlier that part of the increase is due to a longer optical path through the shear layer for oblique propagation.

IV. Controlled Flow

The effects of the actuation strength in terms of the synthetic jet momentum coefficient on the suppression of turbulent energy within the separated flow domain were assessed by varying the jet exit velocity ($C_\mu < 5.6 \times 10^{-4}$) and measuring the corresponding distributions of static pressure. An example of the measured pressure distributions in three planes is shown in Fig. 9 for $\gamma = 139^\circ$ and $M = 0.3$. These data show a clear dependence of streamwise separation delay on the jet momentum coefficient in all three measurement planes and suggests that stronger actuation could lead to additional changes in C_p . The effect of varying the jet momentum coefficient on the spectral properties of the separated flow is demonstrated in Fig. 10 at a fixed cross-stream elevation at all four hot-film measurement stations [$x/R = 0.5$ (HW1), 1 (HW2) 1.5 (HW3), and 2 (HW4)]. As discussed above, direct actuation of small-

scale dissipative motions leads to a significant broadband reduction in turbulent kinetic energy within the wake over the entire streamwise measurement domain. As shown in a planar shear layer by earlier investigations [25], for a given jet momentum coefficient the streamwise suppression of TKE decreases with increasing distance from the control source, which is a direct consequence of the enhanced dissipation within the flow. The present data also indicate that additional reduction can be attained at a higher actuation power (the present measurements are taken at the maximum available actuation level $C_\mu = 5.6 \times 10^{-4}$).

Comparison of the static pressure distributions in the presence and the absence of the actuation shows consistent separation delay effects across the optical aperture, where the magnitude of the separation delay is about 10° at $M = 0.3$. This effect is illustrated in Fig. 11, where static pressure distributions in each of the three measurement planes are shown for $\gamma = 139^\circ$ and $M = 0.3$ and 0.4. In the presence of actuation, alteration of the baseline pressure distributions begins at about 75° , i.e., upstream from the turret apex. Acceleration of the outer flow extends pressure recovery in the downstream direction, which in turn delays separation of the boundary layer. The separation delay effect becomes less pronounced with an increase in M due to the effective decrease in jet momentum coefficient, as can be shown by comparison of the distributions in all three measurement planes for $M = 0.3$ and 0.4. Although separation control typically results in some suppression of turbulent fluctuations in the separated flow, the work of Vukasinovic et al. [25] has shown that dissipative actuation upstream of a separating shear layer off the backward-facing step leads to disruption of the turbulent kinetic energy budget in the ensuing flow. Active suppression of turbulent kinetic energy within the shear layer can be achieved even in the absence of significant separation delay, as it was demonstrated in a shear layer separating from a backward-facing step.

Pressure distributions just upstream of the optical aperture are shown in Fig. 12 for flow conditions in Fig. 11. Both baseline and actuated pressure distributions indicate symmetric pressure

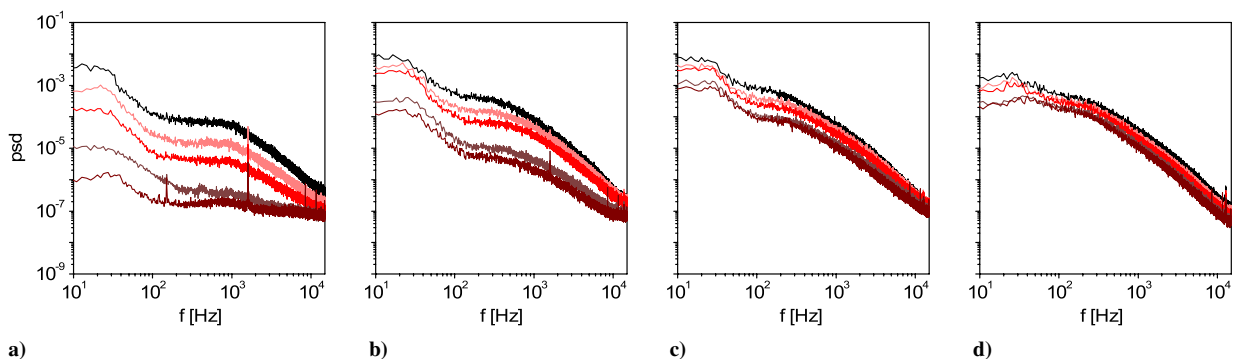


Fig. 10 Power spectra of the velocity fluctuations ($M = 0.3$ and $\gamma = 139^\circ$) for the baseline flow (black) and controlled flows measured by HW1 at a) $y/R = -0.042$, b) HW2 at $y/R = -0.17$, c) HW3 at $y/R = -0.42$, and d) HW4 at $y/R = -0.58$. The spectra of the controlled flow exhibit a decrease in a broadband energy directly proportional to the jet momentum coefficient.

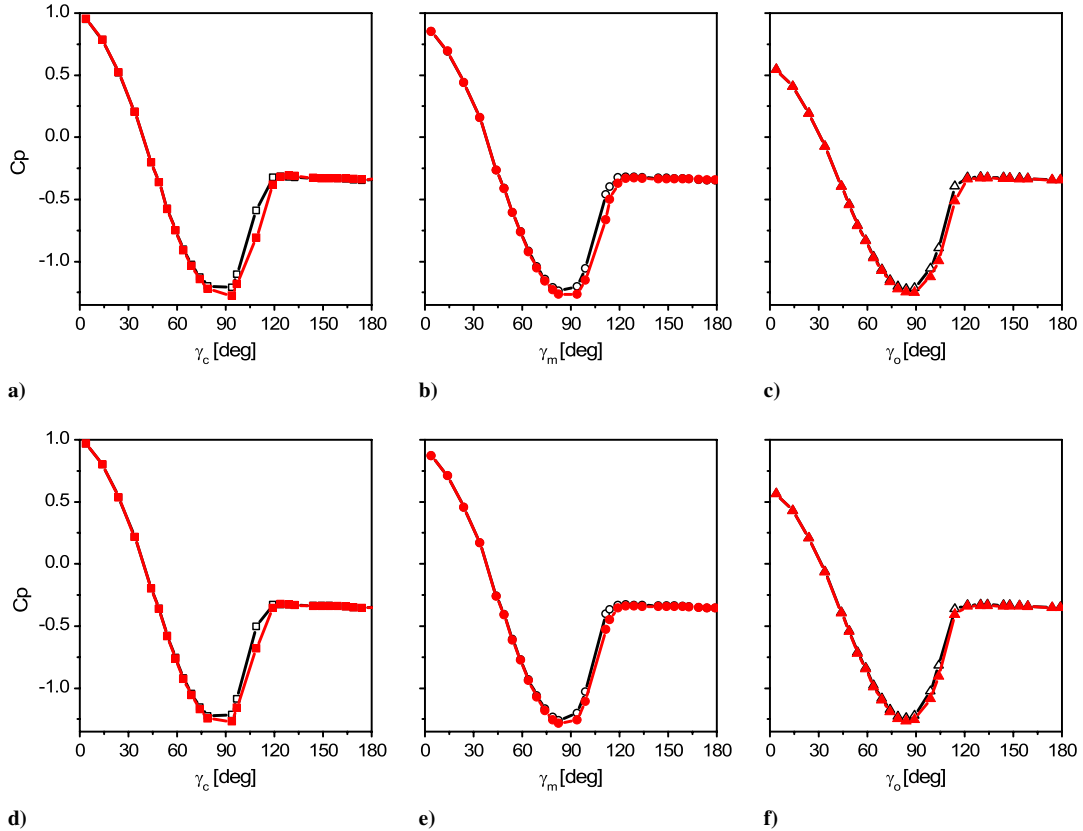


Fig. 11 Static pressure distributions for the baseline (open) and actuated (solid) flows at $\gamma = 139^\circ$ in the central (left column), middle (middle column), and the outer (right column) planes at a–c) $M = 0.3$ and d–f) 0.4 .

distributions about the center plane of the aperture ($\beta = 0^\circ$, Fig. 1). At both Mach numbers, the baseline flow upstream of the aperture is attached and similar to the data shown in Fig. 5 above, the inverted bell-shape profile indicates that the flow first separates at the spanwise edges of the aperture, and the flow over front central part of the aperture remains attached. In the presence of actuation at $M = 0.3$ (Fig. 12a), the largest reduction in pressure is achieved at the center of the aperture but there is a nearly uniform separation delay over approximately the center half of the aperture span. Farther outboard toward the edges of the aperture ($\beta = \pm 57.7^\circ$), there is a sharper decrease in the delay of separation. A similar effect is also seen for $M = 0.4$ (Fig. 12b).

The differences between the baseline and controlled flows are evident from spectra of velocity fluctuations measured using hot-film anemometry. Overall, the spectral analysis shows a significant broadband reduction in the energy of motions within the separated shear layer (it should be pointed out that for a given downstream

position, the energy balance depends on the cross-stream elevation within the shear layer). Figure 13 shows power spectra of velocity fluctuations measured in the central zone of the baseline shear layer at all four measurement locations and among three Mach numbers tested, $M = 0.3, 0.4$, and 0.5 . Closest to the control origin (Fig. 13a), there is a dominant broadband suppression of fluctuation energy at $M = 0.3$; similar, but weaker suppression of energy at large scales at $M = 0.4$, accompanied by an increase in energy at the small-scale motions. Ultimately, an increase in the energy spreads toward the lower frequencies at the highest Mach number flow, and becomes the dominant effect of the flow control. The effect at $M = 0.3$ at the next downstream location (Fig. 13b) is similar to the effect at $M = 0.4$ at the previous location, whereas the effect at $M = 0.4$ is similar to the previous location $M = 0.5$, and so on. Such a pattern is a consistent indicator of the weakening control effect in the downstream direction (due to the dissipation of the control jets), and with the increased freestream speed (due to decreased jet momentum coefficient). By the measurement location HW3 (Fig. 13c), virtually no effect is seen at $M = 0.5$, whereas the flows at $M = 0.3$ and 0.4 exhibit some increase in energy at the small scales and some decrease of energy at the large scales. At the farthest measurement location (Fig. 13d), decrease of the fluctuating energy is still present at $M = 0.3$. Thus, the strongest effect of flow control remains always closest to the control source origin, i.e., over the optical aperture, regardless of the freestream speed.

The effectiveness of a smaller spanwise array of actuators was investigated by comparing the effects of the center 24-element segment of the 36-element actuator array in Fig. 1. The resulting pressure distributions upstream of the optical aperture are shown in Fig. 14 for the aperture elevation angle $\gamma = 137^\circ$ at $M = 0.3, 0.4$, and 0.5 . These data show that in all cases the effect of the smaller actuator array is virtually identical, implying that the outboard actuator segment on each side is not very effective ostensibly due to the influence of the necklace vortices that are involved in the separation of the cylinder support. It is also noted that the actuation effect becomes more localized about the aperture center as M increases.

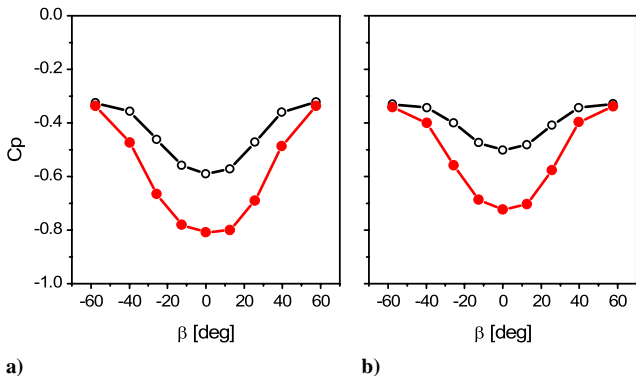


Fig. 12 Pressure distributions about the optical aperture center ($\beta = 0^\circ$) at elevation $\gamma = 139^\circ$ for the baseline flow (open) at actuated (solid) flows at a) $M = 0.3$ and b) 0.4 .

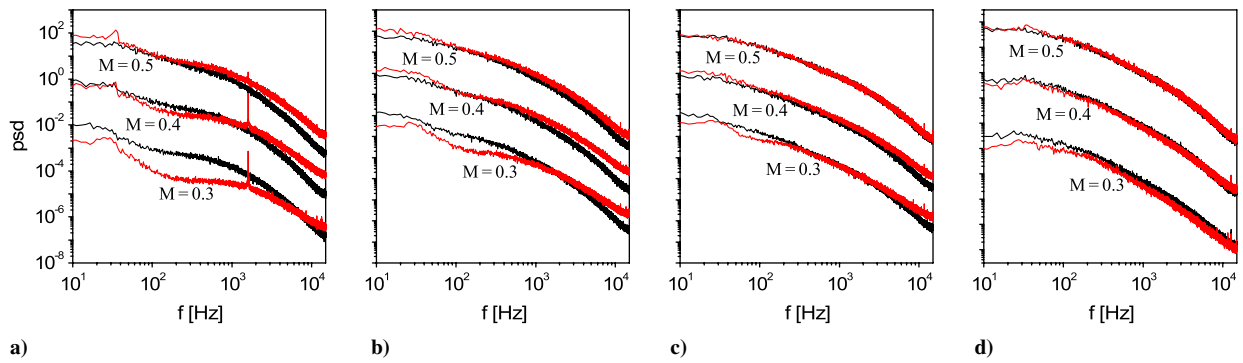


Fig. 13 Power spectra of the velocity fluctuations for the baseline (dark) and actuated (light) flows ($\gamma = 139^\circ$) measured by HW1 at a) $y/R = -0.083$, b) HW2 at $y/R = -0.25$, c) HW3 at $y/R = -0.58$, and d) HW4 at $y/R = -0.75$ for $M = 0.3, 0.4$, and 0.5 .

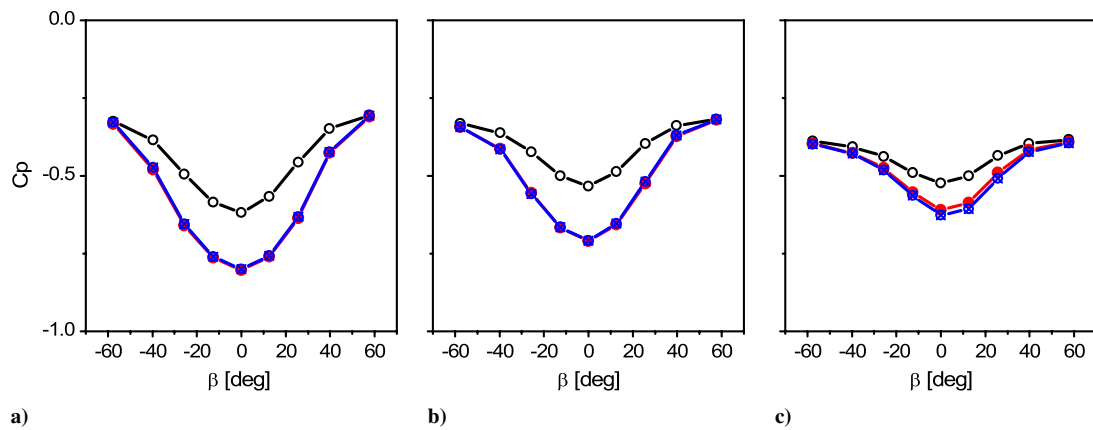


Fig. 14 Pressure distributions about the optical aperture center ($\beta = 0^\circ$) at elevation $\gamma = 137^\circ$ for the baseline (open) at actuated flows by: 36 (solid) and 24 (crossed) element actuator arrays at a) $M = 0.3$, b) 0.4 , and c) 0.5 .

Similarly, the effectiveness of the smaller array actuation is evaluated at three aperture elevation angles $\gamma = 130^\circ, 142^\circ$, and 149° , as shown in Fig. 15. At $\gamma = 130^\circ$ (Fig. 15a), the baseline flow is attached in front of the optical aperture, and the actuation delays separation uniformly across the aperture even with the 24-element array. At $\gamma = 142^\circ$ (Fig. 15b), the baseline flow is separated upstream of the optical aperture, but the actuation delays the separation across the upstream edge of the aperture. At $\gamma = 149^\circ$ (Fig. 15c), the flow remains separated over the upstream edge of the aperture even in the presence of actuation (indicating that the actuation should be applied farther upstream), although, as indicated by the measured velocity spectra, the flow fluctuations within the separated domain are significantly suppressed.

The magnitude of optical distortion that would be encountered by a laser beam emerging from the optical aperture was measured

directly using the MP. Spectra of deflection angles measured in the baseline and actuated flows for the aperture elevation angles $\gamma = 129^\circ, 136^\circ, 143^\circ$, and 148° at $M = 0.3, 0.4$, and 0.5 are shown in Figs. 16–18, respectively. It should be noted (as is evident from these data) that the spectral optical content below 500 Hz is entirely masked by the tunnel environment that, in addition to aero-optical effects, also includes vibrations of the optical hardware and of the model, as already discussed in Sec. III. These vibrations, which are manifested by strong spectral peaks below 500 Hz, completely overwhelm the optical signal and render the raw data unusable at these frequencies for the purpose of active flow control evaluation. However, another control approach in reducing the optical aberrations at these low frequencies could involve both active flow control suppression and adaptive-optics correction of aberrations (including the tip/tilt correction using a fast steering mirror) [26].

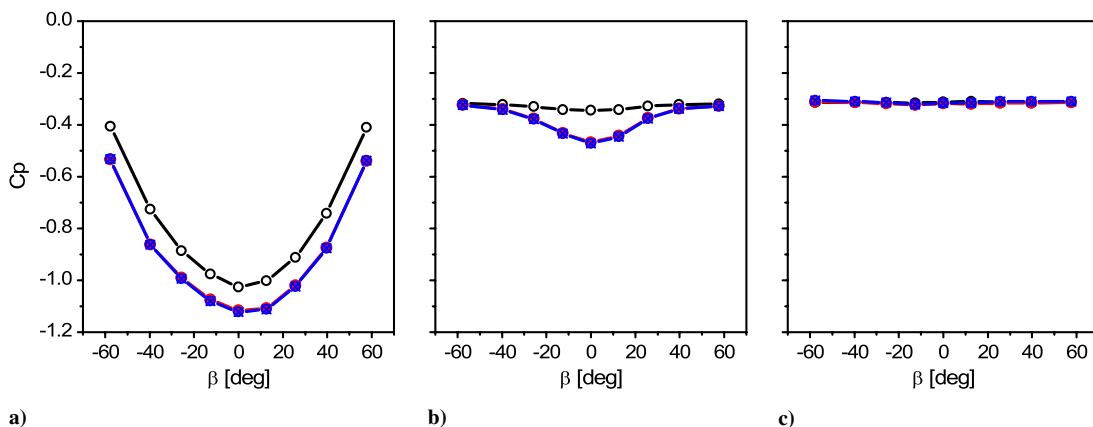


Fig. 15 Pressure distributions about the optical aperture center ($\beta = 0^\circ$) at $M = 0.3$ and elevations a) $\gamma = 130^\circ$, b) 142° , and c) 149° for the baseline (open) and actuated flows using 36 (solid) and 24 (crossed) element actuator arrays.

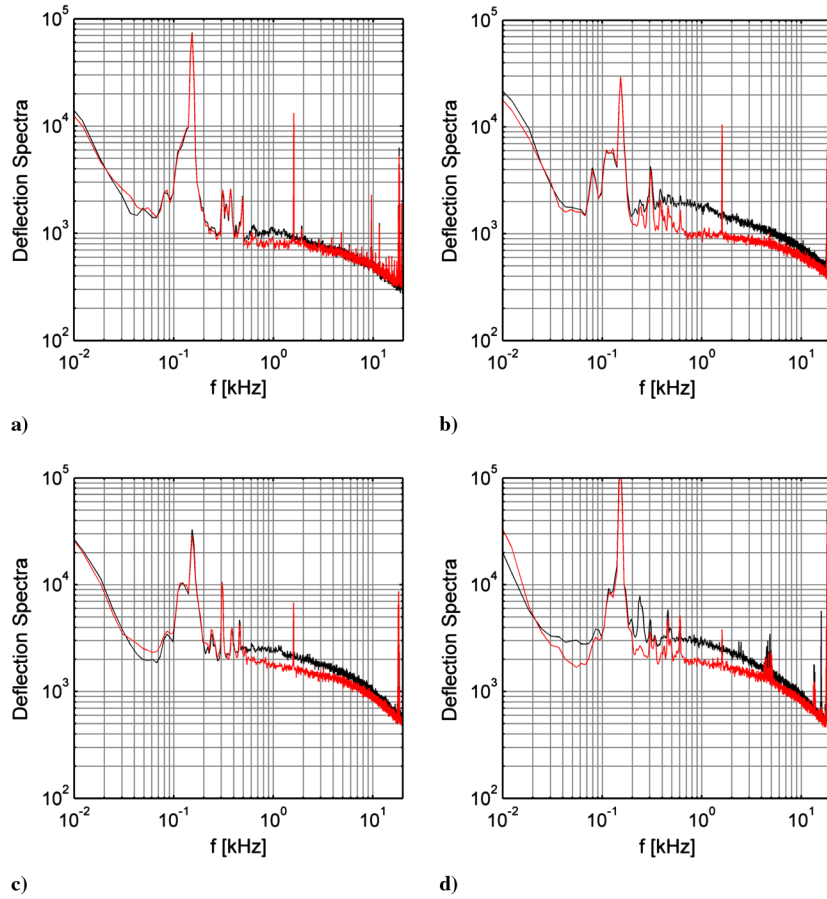


Fig. 16 Spectra of the optical deflection for the baseline (dark) and actuated (light) flows at $M = 0.3$ and a) $\gamma = 129$, b) 136 , c) 143 , and d) 148° .

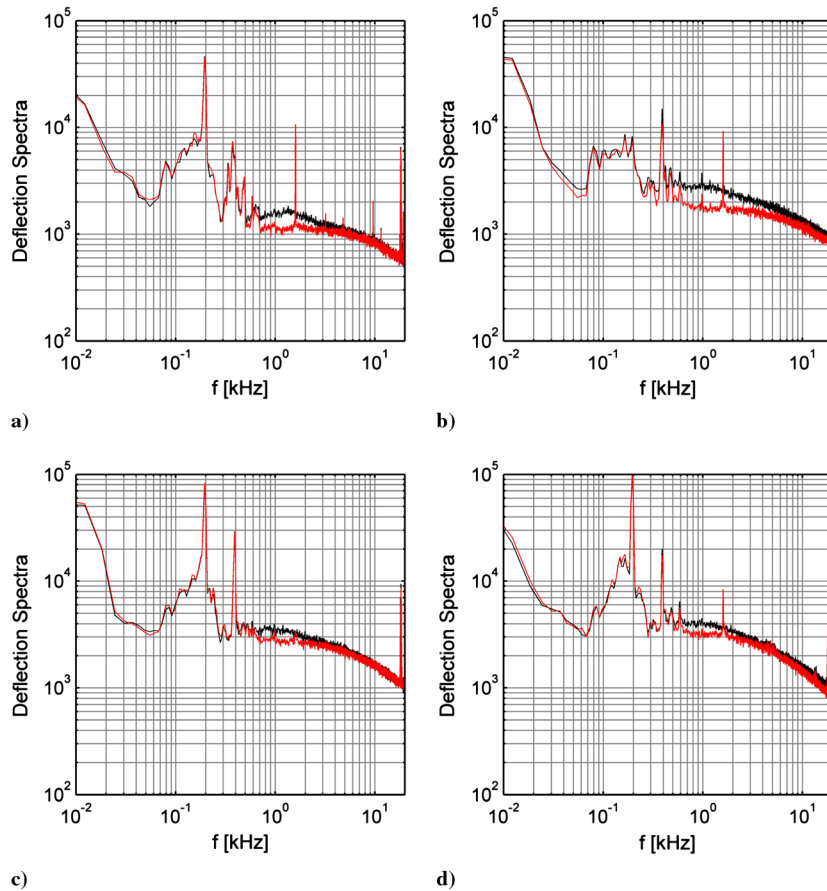


Fig. 17 Spectra of the optical deflection for the baseline (dark) and actuated (light) flows at $M = 0.4$ and a) $\gamma = 129$, b) 136 , c) 143 , and d) 148° .

Assuming that most of the low-frequency aberrations below 500 Hz could be mitigated by the adaptive-optics system, current results can be viewed as additional suppression of optical aberrations beyond the range of optical corrections. In addition, the present MP measurements are taken with a sampling rate of 50 kHz, which imposes an upper frequency band limit around 25 kHz. As a result, the present MP data can only be used to assess effectiveness of the flow control actuation within the band $500 < f < 25,000$ Hz. Except for $\gamma = 143^\circ$ at $M = 0.4$ (Fig. 17c), every actuated spectrum in Figs. 16–18 shows a distinct spike in the actuator-spectra at 1.6 kHz to a greater or lesser extent. This spike indicates that the actuators are introducing well-defined structures into the boundary layer that are responsible for keeping the flow attached (i.e., preventing the separation otherwise present in the baseline flow), and actuation-induced structures induce narrow-band aberrations as will be discussed in more details below. It is noteworthy that the magnitude of this actuation-frequency peak decreases with increasing elevation angle, as the vortical motions that are induced by the actuation dissipate faster within the stronger separated base flow at the higher elevation angles. The most important effect of the actuation-induced small-scale motions on the aero-optical environment around the aperture is the reduction in the energy of the deflection angles within the entire frequency band that is resolved by the MP measurements at all elevation angles. Albeit actuation introduces aberrating structures into the flow at the actuator frequency, the overall effect of the actuation is a broad reduction in the jitter (and concomitant contribution to OPD_{rms}) over the broad frequency range. In particular, the reduction in deflection-angle spectra at frequencies between 0.5 and 10 kHz has the largest effect on the OPD_{rms} (see Appendix A for details). These spectra also demonstrate that the actuation mostly affects frequencies below the actuation frequency of 1.6 kHz and at higher frequencies the actuation spectra are affected less by the actuation and approach the spectra of the baseline. In the present measurements for $M = 0.3$ (Fig. 16), the reduction in spectra of deflection angles is most-significant at $\gamma = 136^\circ$ (Fig. 16b). It is

interesting to note that the smallest suppression is measured at the lowest elevation angle $\gamma = 129^\circ$ (Fig. 16a), but that is attributed to a weak shear layer since the flow separates at about $\gamma_s = 120^\circ$ (Fig. 4a). In addition, since the actuators are fixed within the turret, they are far upstream of the separation for this elevation angle, which makes the shear layer suppression less effective. Finally, it should be noted that the absolute magnitude of the baseline spectrum at $\gamma = 129^\circ$ is about 2 times lower than the corresponding baseline spectrum at $\gamma = 136^\circ$ (Fig. 16b). Similar energy suppression by flow control is also measured at higher Mach number flows, at $M = 0.4$ (Fig. 17) and 0.5 (Fig. 18), but with weakening effectiveness as the actuators' momentum coefficient decreases with increasing M .

Furthermore, it is of interest to quantify the amount of aberration that the introduction of the 1.6 kHz structures has on the optical environment. To address this question, a narrow bandpass filter was placed around each jitter spectrum centered on 1.6 kHz for the case 1 data and the OPD_{rms} computed for only the notched spectra. The contribution of these aberrating structures to overall OPD_{rms} were found to range from 1% to 7% of the no-notch OPD_{rms} . Hence, in the case of $\gamma = 137^\circ$ at $M = 0.3$, for example, the 34% reduction in OPD_{rms} could have been a 41% reduction, had the optical effect from 1.6 kHz aberrating structures been somehow removed, for instance using a feedforward adaptive-optic mitigation procedure [27].

The measured deflection spectra were high-pass filtered below 500 Hz using a filter described in Appendix A and levels of optical distortion, OPD_{rms} , were calculated as discussed in Sec. II and Appendix A for each actuation case and compared to the corresponding baseline flow. The error analysis of the results gave approximately 10% of the relative error for all optical results, mostly due to the accuracy of the measurement of the Malley probe beams' separation. Figure 19 shows the comparison of the case 1 actuation to the baseline for each elevation angle and all three Mach numbers in a nondimensional form. A common feature is that the actuation yielded suppression in optical aberrations for all flow conditions. It should be also noted that in many cases the improvement over the baseline was

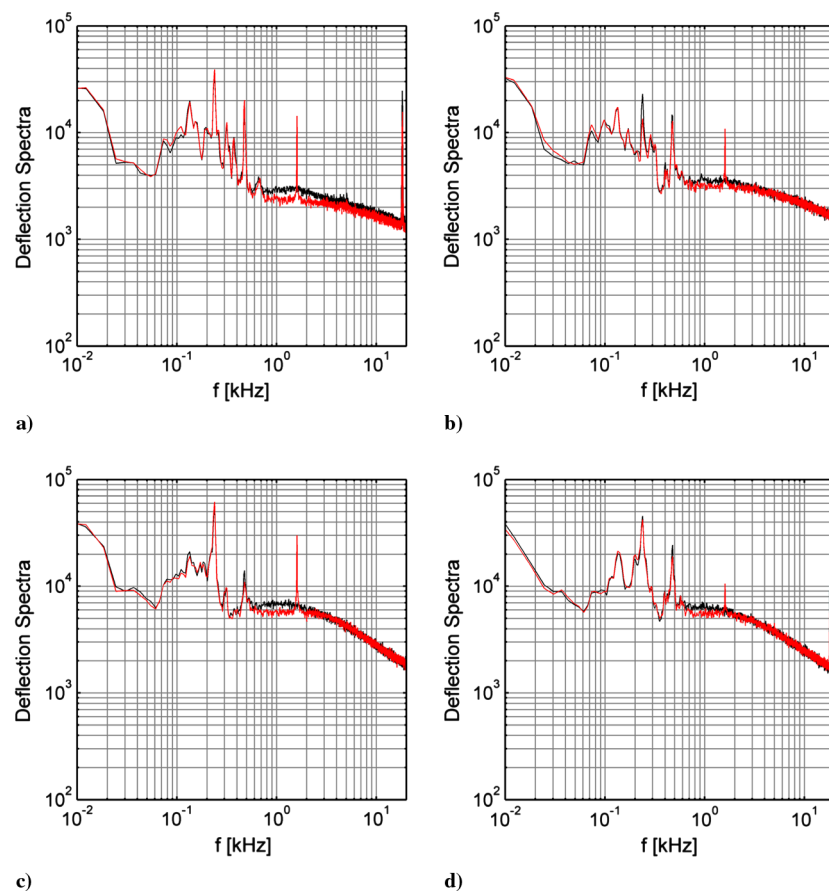


Fig. 18 Spectra of the optical deflection for the baseline (dark) and actuated (light) flows at $M = 0.5$ and a) $\gamma = 129^\circ$, b) 136° , c) 143° , and d) 148° .

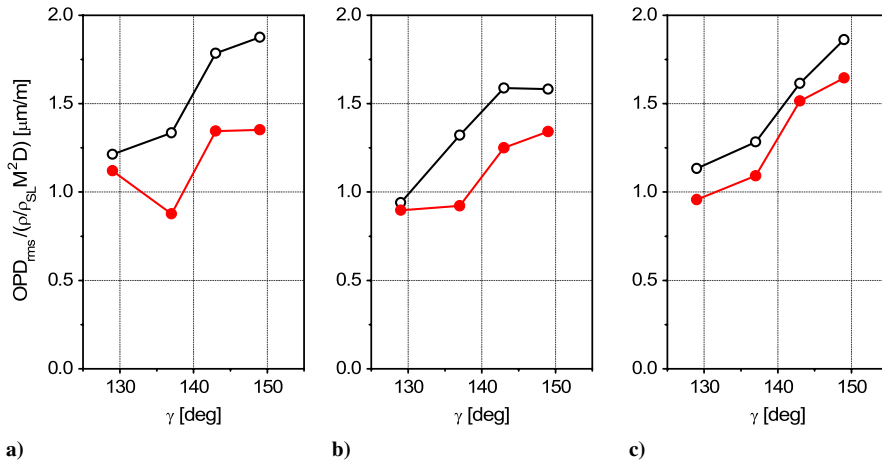


Fig. 19 Normalized baseline (open) and controlled-flow (solid, case 1) optical data, $OPD_{rms} / (\rho M^2 D)$, as a function of elevation angle γ for all Mach numbers a) $M = 0.3$, b) 0.4 , and c) 0.5 .

quite large. At $M = 0.3$, the reduction in OPD_{rms} at $\gamma = 137^\circ$, for example, for case 1 yielded a 34% improvement and at $M = 0.4$ the improvement dropped by only 4% to a 30% improvement. This reduction in OPD_{rms} is even more significant to the far-field intensity, since the far-field intensity improvement for large apertures goes approximately as

$$\frac{I}{I_0} = \exp\left\{-\left(\frac{2\pi OPD_{rms}}{\lambda}\right)^2\right\}$$

where I is the on axis intensity after tilt removal, divided by the diffraction-limited intensity, I_0 , and λ is the laser wavelength.

All the results are presented in Table 1, where actuation using the full set of actuators is labeled as case 1, and spanwise-limited actuation using the 24 central actuators is labeled as case 2. Full actuation (case 1) was tested at all four aperture elevation angles and at each Mach number, and case 2 was tested at two elevation angles for $M = 0.3$ and 0.4 , and one elevation angle at $M = 0.5$. As already discussed in conjunction with Fig. 16, the smallest *relative* improvement in optical distortions within the present spectral band is measured at the lowest elevation angle at $M = 0.3$, but significant suppression is measured at all other elevation angles where the shear layer over the optical aperture is more developed. Very similar, but slightly weaker effects on aberration suppression are achieved at $M = 0.4$. The overall effect weakens further at the highest Mach number flow of $M = 0.5$, but the bandwidth-limited measured suppression is still notable. When assessing impact of the reduced spatial distribution of actuators, by comparing cases 1 and 2, no significant difference is observed, as the measured suppression by the spanwise-limited distribution of actuators is either slightly weaker, or even slightly stronger than in the case of full actuation. This finding suggests a possible redistribution of the control sources for future tests. It should also be pointed out that although the active flow

control at $M = 0.3$ and $\gamma = 149^\circ$ does not effect the separation off the turret (see Fig. 15c), measured aberration by the Malley probe indicate the resulting suppression of optical aberration of about 30% (Table 1). This finding shows that the effect of fluidic active flow control on optical aberration is not exclusively expressed through separation delay, but it induces an active suppression of turbulent fluctuations even in the absence of separation delay.

V. Conclusions

The effectiveness of direct, dissipative small-scale actuation for suppression of optical aberrations within the separated flow over a conformal optical aperture mounted within the hemispherical cap of a cylindrical turret model is investigated at $M = 0.3$ and $Re_D = 4.46 \cdot 10^6$, with additional tests done at $M = 0.4$ and 0.5 . The effects of actuation on the base flow at several elevation angles of the optical aperture are assessed from surface oil visualization, static pressure distributions, and hot-film measurements within the separated flow domain. Suppression of optical distortions across the separated flow is evaluated directly using the Malley probe sensor.

The topology of the baseline flow at $M = 0.3$ indicates that the near-wake flow is dominated by the separation behind the hemispherical cap of the turret. The flow separates first near the outer spanwise edges of the hemisphere, and the separation progresses toward the center plane, so that the flow remains attached farthest along the plane of symmetry. The separated wake downstream of the turret reattaches to the base plane of the turret at a nominal distance of $1.3R$ downstream from its downstream juncture. Surface oil visualization has shown that the recirculating flow domain is bounded along its spanwise edges by two separate, narrower, recirculating domains that are induced by separation off the turret's cylinder support. The flow separation along the cylinder support is amplified by interaction with the necklace vortex that forms at the juncture between the cylinder and the support plane.

Direct small-scale dissipative actuation using arrays of streamwise rectangular synthetic jets mounted around the upstream perimeter of the optical aperture leads to significant separation delay on the aperture's surface. The extent of the separation delay varies with the elevation angle γ of the aperture, and can extend up to 10° at $\gamma = 139^\circ$. Furthermore (and perhaps more importantly), spectra of the streamwise velocity fluctuations show that the dissipative actuation results in a substantial broadband suppression of the turbulent kinetic energy within the near wake and, in particular, the energy that is associated with large coherent vortical structures. Although this attenuation is not a direct measure of the reduction in aero-optical aberrations, it is indicative of the overall reduction in the characteristic length scales within the separated flow domain. Direct optical measurements at a freestream Mach number $M = 0.3$ show that the actuation leads to a suppression of at least 30% in optical aberration as measured within the frequency band $0.5 < f < 25$ kHz (at the low

Table 1 Relative improvement in optical distortions OPD_{rms} for the actuated flows relative to the baseline flows for different elevation angles γ

	γ , deg			
	129	136	143	149
$M = 0.3$				
Case 1	8%	34%	24%	28%
Case 2	—	31%	—	37%
$M = 0.4$				
Case 1	5%	30%	21%	15%
Case 2	—	—	24%	12%
$M = 0.5$				
Case 1	20%	15%	6%	12%
Case 2	—	12%	—	—

end this band is limited by the tunnel's optical contamination and vibrations). Under the assumption that any existing aberrations below the lower limit of 500 Hz could be mitigated by means of a conventional adaptive-optic system, the current results can be viewed as additional suppression of optical aberrations beyond the range of optical corrections. The broadband turbulent energy suppression that is evident from hot-film velocity spectra suggests that the actual reduction in optical aberrations may be higher. Additional measurements at $M = 0.4$ and 0.5 show similar trends albeit somewhat less effective in terms of separation delay and suppression of optical aberrations. The actuation effects at these higher Mach numbers are apparently limited by the strength of the present actuators and the precipitous decrease in jet momentum coefficient with Mach number. The suppression of optical aberrations (beyond the adaptive-optics correction) is at least 20 and 10% for freestream Mach numbers $M = 0.4, 0.5$, respectively. It is noteworthy that the same suppression of optical aberrations was attained with the central 2/3 subset of the jet actuator array upstream of the optical aperture and therefore with about 2/3 of the actuation power. Finally, as the structures introduced into the flow by the actuation are so narrowly centered at the actuation frequency, it is believed that they could be removed using a feedforward, adaptive-optics approach similar to that demonstrated with a regularized shear layer [27].

Appendix A: Relation Between Deflection-Angle Spectra and OPD_{rms}

Mechanically induced vibrations from the tunnel motor impose significant amounts of contamination at the low-frequency end of the deflection-angle spectra and partially corrupt the aero-optical signal. To remove this mechanical-vibration corruption, one needs to know the correct, uncorrupted behavior of the deflection-angle spectrum at the low-frequency end to properly filter it out.

To derive a proper high-pass filter, it is helpful to revisit how Malley probe data are used to construct a meaningful optical figure of merit. Malley probes measure 1-D jitter/deflection-angle spectra, $P_\theta(f) = \langle \hat{\theta}(f)\hat{\theta}^*(f) \rangle$, but a typical figure of merit for aero-optics is the OPD_{rms} for a given aperture size, Ap . These quantities are related as follows: Since the square of the RMS Optical Path Difference is identical to the square of the RMS wave-front distortion from its mean, i.e., $OPD_{rms}^2 \equiv W_{rms}^2$, the OPD_{rms} is related to the 1-D wave-front power spectrum, $P_W(k) = \langle \hat{W}(k)\hat{W}^*(k) \rangle$, as

$$OPD_{rms}^2 \equiv \frac{1}{2\pi} \int_{-\infty}^{\infty} P_W(k) dk \quad (A1)$$

where $\hat{W}(k)$ is the Fourier transform of a 1-D wave-front distortion, $W(x)$. However, the jitter/deflection angle θ is the spatial derivative in the streamwise direction of the wave front:

$$\theta(x = U_c t) = \frac{dW(x = -U_c t)}{dx} = -\frac{1}{U_c} \frac{dW(t)}{dt}$$

Here, the frozen-flow convective hypothesis is applied with U_c being the convective speed. So the wave-front power spectrum can be computed from the deflection-angle power spectrum, as

$$P_W(f) = \left(\frac{U_c}{2\pi f}\right)^2 P_\theta(f)$$

Substituting this expression into Eq. (A1), we get

$$\begin{aligned} OPD_{rms}^2 &= \frac{1}{2\pi} \int_{-\infty}^{\infty} P_W(k) dk = \int_{-\infty}^{\infty} P_W(f) df \\ &= \int_{-\infty}^{\infty} \left(\frac{U_c}{2\pi f}\right)^2 P_\theta(f) df = U_c^2 \int_{-\infty}^{\infty} \frac{P_\theta(f)}{(2\pi f)^2} df \end{aligned}$$

The derived expression is valid only for an infinite aperture. It was shown that for finite apertures [28,29], the above expression should be modified by including a 1-D aperture filter $AF(Ap, f)$ (see Fig. A1a):

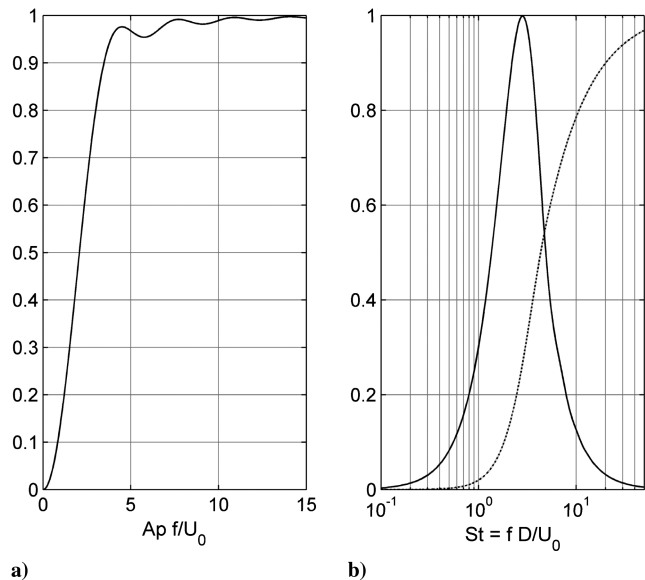


Fig. A1 Plots of a) aperture filter $AF(Ap, f)$ and b) optical filter transfer $G(f)$ (solid line) and cumulative $CG(f)$ (dashed line) function.

$$\begin{aligned} OPD_{rms}^2(Ap) &= U_c^2 \int_{-\infty}^{\infty} AF(Ap, f) \frac{P_\theta(f)}{(2\pi f)^2} df \\ &= \int_0^{\infty} G(Ap, f) P_\theta(f) df \end{aligned} \quad (A2)$$

where

$$G(Ap, f) = \frac{2U_c^2}{(2\pi f)^2} AF(Ap, f)$$

is a transfer function between the deflection-angle spectrum and the apertured $OPD_{rms}(Ap)$. Figure A1b shows the transfer function, $G(f)$, as a function of $St = fD/U_0$, where D is a turret diameter and U_0 is the freestream speed (as the convective speed U_c was measured as to be approximately U_0). As easily observed in Fig. A1b, the transfer function, $G(f)$, is a bandpass filter, centered about $St = 3$. The low-frequency cutoff is due to aperture effects, in which very low frequencies are present inside the aperture mostly as tip/tilt and therefore are removed from the final result under the presumption that a fast steering mirror would be present in the beam-control system for a laser [28]. The high-frequency cutoff is due to the integral relation between the jitter/deflection-angle signal and the

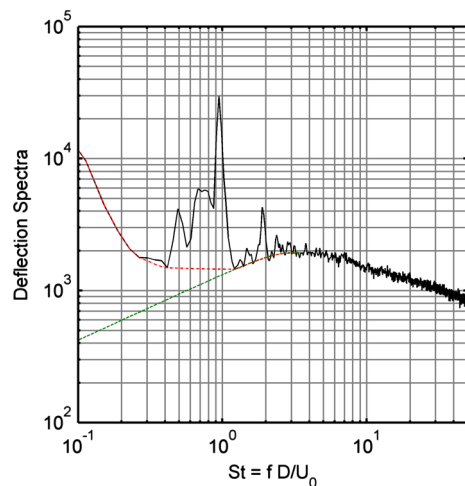


Fig. A2 Deflection-angle spectrum for the baseline flow ($M = 0.3$ and $\gamma = 137^\circ$): unfiltered (solid line) and with applied low-pass filter 1 (lower dashed line) and filter 2 (upper dashed line).

wave front. Therefore, Eq. (A2) shows that the measured optical quantity, the jitter/deflection-angle spectrum, should be, in effect, *bandpass-filtered* in order to calculate the level of aero-optical aberrations OPD_{rms} for a given aperture size.

The normalized cumulative transfer function,

$$CG(f) = \frac{\int_0^f G(x) dx}{\int_0^\infty G(x) dx}$$

is also plotted in Fig. A1b. It is clear that for this aperture, 95% of the filtered energy is located between $St = 1$ and 60. Therefore, the exact shape of the low-pass filter (or more accurately, the fit) that is applied to the measured deflection angles to compensate for vibration contamination is in fact *irrelevant* below $St = 1$ (and above $St = 60$) as long as all nonphysical components, such as vibrations, are removed or highly suppressed by the empirical low-pass filter. Direct numerical calculations confirm these results. Two different filters were applied to remove vibration-related low frequencies (see Fig. A2). The resulting OPD_{rms} after applying these two filters differ by less than 6%. So all data reported below were processed by applying filter 1.

High-pass filter 1, $F(f)$, was constructed as follows:

$$F(f) = \begin{cases} \frac{P_\theta(f_{peak})(f/f_{peak})^n}{P_\theta(f)} & f < f_{peak} \\ 1 & f \geq f_{peak} \end{cases}$$

The cutoff frequency was chosen to be $f_{peak}D/U_0 = 2.0$. The filter was then applied to the time-dependent data as discussed earlier. Several values of n between 1 and 2 were tested and it was found that the resulting apertured OPD_{rms} did not change much, so the conservative value of $n = 1$ was chosen for the high-pass filter $F(f)$.

Acknowledgments

This work has been supported by the U.S. Air Force Research Laboratory (AFRL), Air Vehicle Directorate, Wright-Patterson Air Force Base, Ohio, and the Boeing Company. Support by the AFRL Program Manager Donnie Saunders and Subsonic Aerodynamic Research Laboratory tunnel personnel is greatly appreciated.

References

- [1] Sutton, G., "Aero-Optical Foundations and Applications," *AIAA Journal*, Vol. 23, 1985, pp. 1525–1537. doi:10.2514/3.9120
- [2] Gordeyev, S., Hayden, T., and Jumper, E., "Aero-Optical and Flow Measurements over a Flat-Windowed Turret," *AIAA Journal*, Vol. 45, No. 2, 2007, pp. 347–357. doi:10.2514/1.24468
- [3] Gordeyev, S., Post, M., MacLaughlin, T., Ceniceros, J., and Jumper, E., "Aero-Optical Environment Around a Conformal-Window Turret," *AIAA Journal*, Vol. 45, No. 7, 2007, pp. 1514–1524. doi:10.2514/1.26380
- [4] Gilbert, J., and Otten, L. J. (eds.), *Aero-Optical Phenomena*, Progress in Astronautics and Aeronautics, Vol. 80, AIAA, New York, 1982.
- [5] Tatarskii, V. I., and Zavorotnyi, V. U., "Wave Propagation in Random Media with Fluctuating Turbulent Parameters," *Journal of the Optical Society of America*, Vol. 2, No. 12, 1985, pp. 2069–2076. doi:10.1364/JOSAA.2.002069
- [6] Jumper, E. J., and Fitzgerald, E. J., "Recent Advances in Aero-Optics," *Progress in Aerospace Sciences*, Vol. 37, 2001, pp. 299–339. doi:10.1016/S0376-0421(01)00008-2
- [7] Fitzgerald, E. J., and Jumper, E. J., "The Optical Distortion Mechanism in a Nearly Incompressible Free Shear Layer," *Journal of Fluid Mechanics*, Vol. 512, 2004, pp. 153–189. doi:10.1017/S0022112004009553
- [8] Smith, D. R., Amitay, M., Kibens, V., Parekh, D., and Glezer, A., "Modification of Lifting Body Aerodynamics Using Synthetic Jet Actuators," AIAA Paper 1998-0209, 1998.
- [9] Amitay, M., and Glezer, A., "Role of Actuation Frequency in Controlled Flow Reattachment over a Stalled Airfoil," *AIAA Journal*, Vol. 40, 2002, pp. 209–216. doi:10.2514/2.1662
- [10] de Jonckheere, R., Russell, J. J., and Chou, D. C., "High Subsonic Flowfield Measurements and Turbulent Flow Analysis Around a Turret Protuberance," AIAA Paper 82-0057, 1982.
- [11] Cress, J., Gordeyev, S., Jumper, E., Ng, T., and Cain, A., "Similarities and Differences in Aero-Optical Structure over Cylindrical and Hemispherical Turrets with a Flat Window," AIAA Paper 2007-0326, 2007.
- [12] Purohit, S. C., Shang, J. S., and Hankey, W. L., "Effect of Suction on the Wake Structure of a Three-Dimensional Turret," AIAA Paper 83-1738, 1983.
- [13] Snyder, C. H., Franke, M. E., and Masquelier, M. L., "Wind-Tunnel Tests of an Aircraft Turret Model," *Journal of Aircraft*, Vol. 37, 2000, pp. 368–376. doi:10.2514/2.2625
- [14] Gordeyev, S., Jumper, E. J., Ng, T. T., and Cain, A. B., "The Optical Environment of a Cylindrical Turret with a Flat Window and the Impact of Passive Control Devices," AIAA Paper 2005-4657, 2005.
- [15] Manhart, M., "Vortex Shedding From a Hemisphere in a Turbulent Boundary Layer," *Theoretical and Computational Fluid Dynamics*, Vol. 12, 1998, pp. 1–28. doi:10.1007/s001620050096
- [16] Leder, A., Grebin, U., Hassel, E., Kashkoul, Y., and Ackl, A., "3-D-Flow Structures Behind a Circular Cylinder with Hemispherical Head Geometry," *Proceedings in Applied Mathematics and Mechanics*, Vol. 3, 2003, pp. 40–43.
- [17] Vukasinovic, B., Brzozowski, D., and Glezer, A., "Fluidic Control of Separation over a Hemispherical Turret," *AIAA Journal*, Vol. 47, No. 9, 2009, pp. 2212–2222. doi:10.2514/1.41920
- [18] Vukasinovic, B., Glezer, A., Gordeyev, S., Jumper, E., and Kibens, V., "Active Control and Optical Diagnostics of the Flow over a Hemispherical Turret," AIAA Paper 2008-0598, 2008.
- [19] Woszidlo, R., Taubert, L., and Wagnanski, I., "Manipulating the Flow over Spherical Protuberances in a Turbulent Boundary Layer," *AIAA Journal*, Vol. 47, 2009, pp. 437–450. doi:10.2514/1.39930
- [20] Vukasinovic, B., and Glezer, A., "Control of a Separating Flow over a Turret," AIAA Paper 2007-4506, 2007.
- [21] Morgan, P. E., and Visbal, M. R., "Numerical Simulations Investigating Control of Flow over a Turret," AIAA Paper 2009-574, 2009.
- [22] Andino, M. Y., Wallace, R. D., Glauser, M. N., Schmit, R. F., Myatt, J. H., and Camphouse, R. C., "Flow and Aero-Optics Around a Turret. Part 1. Open Loop Flow Control," AIAA Paper 2008-4216, 2008.
- [23] Wallace, R. D., Andino, M. Y., Glauser, M. N., Camphouse, R. C., Schmit, R., and Myatt, J. H., "Flow and Aero-Optics Around a Turret. Part 2. Surface Pressure Based Proportional Closed Loop Flow Control," AIAA Paper 2008-4217, 2008.
- [24] Wallace, R., Andino, M., Glauser, M., Camphouse, C., Schmit, R., and Myatt, J., "Flow Characteristics of Active Control Around a 3-D Turret," AIAA Paper 2009-573, 2009.
- [25] Vukasinovic, B., Glezer, A., and Rusak, Z., "Experimental and Numerical Investigation of Controlled, Small-Scale Motions in a Turbulent Shear Layer," *Proceedings of the 3rd International Symposium of Integrating CFD and Experiments in Aerodynamics*, June 2007.
- [26] Tyson, R. K., *Principles of Adaptive Optics*, 2nd ed., Academic Press, Chestnut Hill, MA, 1991.
- [27] Nightingale, A., Mitchell, B., Goodwine, B., and Jumper, E., "Feedforward Adaptive-Optic Mitigation of Aero-Optic Disturbances," AIAA Paper 2008-4211, 2008.
- [28] Siegenthaler, J. P., Gordeyev, S., and Jumper, E., "Shear Layers and Aperture Effects for Aero-Optics," AIAA Paper 2005-4772, 2005.
- [29] Siegenthaler, J. P., "Guidelines for Adaptive-Optic Correction Based on Aperture Filtration," Ph.D. Dissertation, Univ. of Notre Dame, Notre Dame, IN, Dec. 2008.

M. Glauser
Associate Editor